Geophysical Research Letters

RESEARCH LETTER

10.1029/2026GL121737

Multi-Stage Shallow Rupture and Pre-Event Shallow Deformation During the 2025 Mw 5.9 Asadabad Earthquake (Afghanistan)

Ping He[1,2], Timothy J. Craig[2], Yangmao Wen[3], Huihui Weng[4], Kefeng He[3], and Caijun Xu[3]

[1]School of Geophysics and Geomatics, China University of Geosciences, Wuhan, China, [2]COMET, School of Earth and Environment, University of Leeds, Leeds, UK, [3]School of Geodesy and Geomatics, Wuhan University, Wuhan, China, [4]State Key Laboratory for Mineral Deposits Research, School of Earth Sciences and Engineering, Nanjing University, Nanjing, China

Key Points:

- InSAR and teleseismic waveforms reveal the spatial and temporal evolution of the mainshock and three aftershocks
- The rupture involved a multi-stage shallow sequence on unmapped, high-dip faults, with a blind mainshock and surface-reaching segments
- Time-series InSAR shows ~2 mm/yr pre-event uplift in the epicentral area, suggesting preparatory deformation prior to the earthquake

Supporting Information:

Supporting Information may be found in the online version of this article.

Correspondence to:

P. He,
phe@cug.edu.cn

Citation:

He, P., Craig, T. J., Wen, Y., Weng, H., He, K., & Xu, C. (2026). Multi-stage shallow rupture and pre-event shallow deformation during the 2025 Mw 5.9 Asadabad earthquake (Afghanistan). *Geophysical Research Letters*, *53*, e2026GL121737. https://doi.org/10.1029/2026GL121737

Received 12 JAN 2026
Accepted 18 APR 2026

Author Contributions:

Conceptualization: Ping He, Yangmao Wen
Funding acquisition: Ping He, Yangmao Wen
Investigation: Ping He
Methodology: Ping He, Timothy J. Craig
Software: Ping He, Timothy J. Craig, Yangmao Wen, Kefeng He
Validation: Ping He, Timothy J. Craig, Yangmao Wen
Visualization: Ping He, Timothy J. Craig
Writing – original draft: Ping He
Writing – review & editing: Ping He, Timothy J. Craig, Yangmao Wen, Huihui Weng, Kefeng He, Caijun Xu

Abstract The 31 August 2025 Mw 5.9 Asadabad earthquake in eastern Afghanistan caused severe damage despite its moderate magnitude, raising questions about rupture processes and seismic hazard in the southern Hindu Kush. Using Sentinel-1 InSAR and teleseismic waveform modeling, we reveal a complex, multi-stage shallow (4–5 km) rupture involving the mainshock and three M > 5.0 aftershocks. Surface deformation ranges from ~10 to 35 cm, and fault planes exhibit moderate to steep dip angles, with secondary rupture approaching the surface. Time-series InSAR shows ~2 mm/yr localized interseismic uplift near the epicenter, consistent with localized shallow deformation prior to the earthquake. Occurring within exposed crystalline basement rocks without mapped Quaternary faults, the earthquake ruptured a previously unknown immature, distributed fault system. These findings help explain the high damage relative to magnitude and highlight significant seismic hazard in orogenic interiors from moderate-magnitude, shallow ruptures on unmapped faults.

Plain Language Summary On 31 August 2025, a moderate earthquake (Mw 5.9) struck near Asadabad, Afghanistan, causing severe destruction and over 2200 fatalities. Investigations show the quake involved several shallow fault breaks, with some ruptures reaching close to the surface, leading to high-intensity ground shaking. Satellite observations also reveal slow uplift in the epicentral area before the event, suggesting localized crustal deformation prior to the earthquake. The earthquake occurred on previously unmapped faults within hard basement rocks, rather than on well-known active faults. This hidden, distributed fault system helps explain why moderate shaking to produce unexpectedly severe damage. The study highlights that earthquakes in mountainous regions can be highly destructive even at moderate magnitudes, and that traditional hazard assessments based only on earthquake size may underestimate risks from shallow, unmapped faults.

1. Introduction

The 31 August 2025 Mw 5.9 Asadabad earthquake occurred in eastern Afghanistan within the southern Hindu Kush, the westernmost segment of the oblique India–Eurasia collision zone, where convergence proceeds at ~39 mm/yr (e.g., Kapp & DeCelles, 2019; Tapponnier et al., 2001; Yin & Harrison, 2000) (Figure 1). Seismicity here reflects compressive forces generated by the northward motion of India toward Central Asia, with the overall convergence rate accommodated by a combination of the underthrusting of the Indian plate beneath Eurasia, and intraplate compression within the orogenic belts of Asia (Kufner et al., 2017, 2021; Sippl et al., 2013). Regional upper-crustal deformation is characterized by NW–SE contraction and lateral extrusion, partitioned among major strike-slip systems (e.g., the Chaman and Herat faults) and a network of transpressional structures toward the northeast, including the Kunar fault (Mohadjer et al., 2016; Ruleman et al., 2007). Despite this tectonic complexity, many active faults remain poorly constrained.

According to the United States (USGS, 2025), the earthquake was reported as M 6.0, with an epicenter at 34.706°N, 70.793°E and a focal depth of ~8 km. The mainshock was followed by a dense aftershock sequence over the subsequent 5 days, including six events of magnitude M ≥ 5.0, the largest being an M 5.6 earthquake on 4 September (Figure 1; Table S1 in Supporting Information S1). For clarity, hereinafter M denotes catalog magnitudes reported by the USGS, whereas Mw refers to moment magnitudes derived from our geodetic and

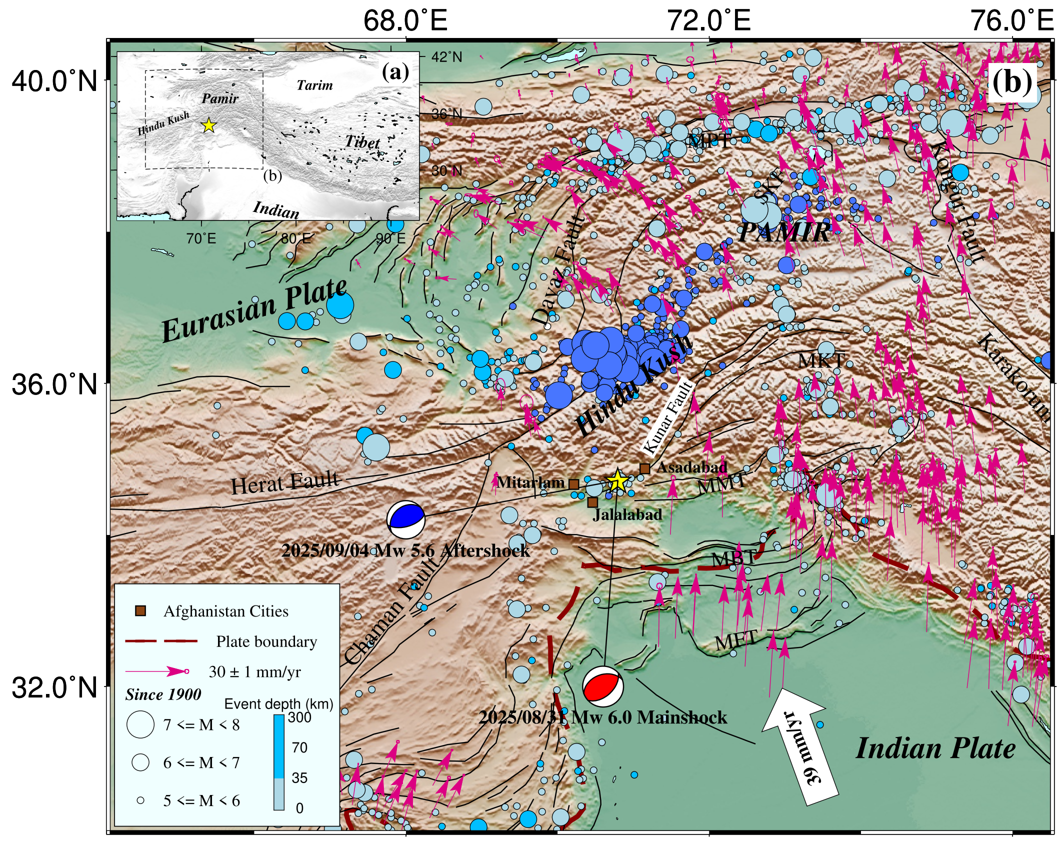

Figure 1. Tectonic setting of the westernmost Himalayan collision zone and the epicenters of the 2025 Mw 5.9 Asadabad earthquake sequence. (a) Inset showing a broader regional view to locate the study area within the India–Eurasia collision zone. (b) Detailed view of the epicentral region. Colored circles indicate earthquakes since 1900 from the USGS catalog (USGS, 2025). Black lines represent active faults from the Global Earthquake Model database (Styron & Pagani, 2020). Dark red lines denote plate boundaries, and white arrows show the relative motion between the Indian and Eurasian plates (Shnizai, 2020). Magenta arrows indicate interseismic GNSS velocity vectors from previous studies (Rollins, 2023). Beach balls show preliminary focal mechanisms of the mainshock and the largest aftershock (Mw 5.6) reported by the USGS. Dark red squares mark major cities in the epicentral region.

seismological modeling. Despite its moderate magnitude, the mainshock caused severe impacts, including more than 2,200 fatalities, widespread structural collapse, and extensive damage, making it one of the deadliest earthquakes in Afghanistan in recent decades (Kufner et al., 2023; NOAA, 2023; WHO, 2025).

The severity of damage, given the moderate magnitude, suggests that several geological and structural factors may have amplified the earthquake's impact. Understanding the rupture processes, multi-fault interactions, and the role of shallow slip is therefore critical for assessing seismic hazard in this complex region. However, the sparse regional seismic network limits conventional source analyses. To overcome these limitations, we combine geodetic measurements and teleseismic waveform modeling to characterize the rupture process and evaluate the mechanisms responsible for the earthquake's unexpectedly high impact.

2. Data and Methods

2.1. InSAR Data

We used Sentinel-1 TOPS-mode SAR data from two ascending (T173A, T071A) and two descending (T005D, T078D) tracks to capture coseismic deformation (Figure 2). Interferograms isolate deformation from the mainshock, the M 5.6 aftershock, and the cumulative sequence (USGS, 2025; Table S2 in Supporting Information S1). Interferograms were processed followed standard GAMMA workflows (Wegnüller et al., 2016). Topographic phase contributions were removed using the 30-m Copernicus Digital Elevation Model (DEM) (ESA, 2023), and

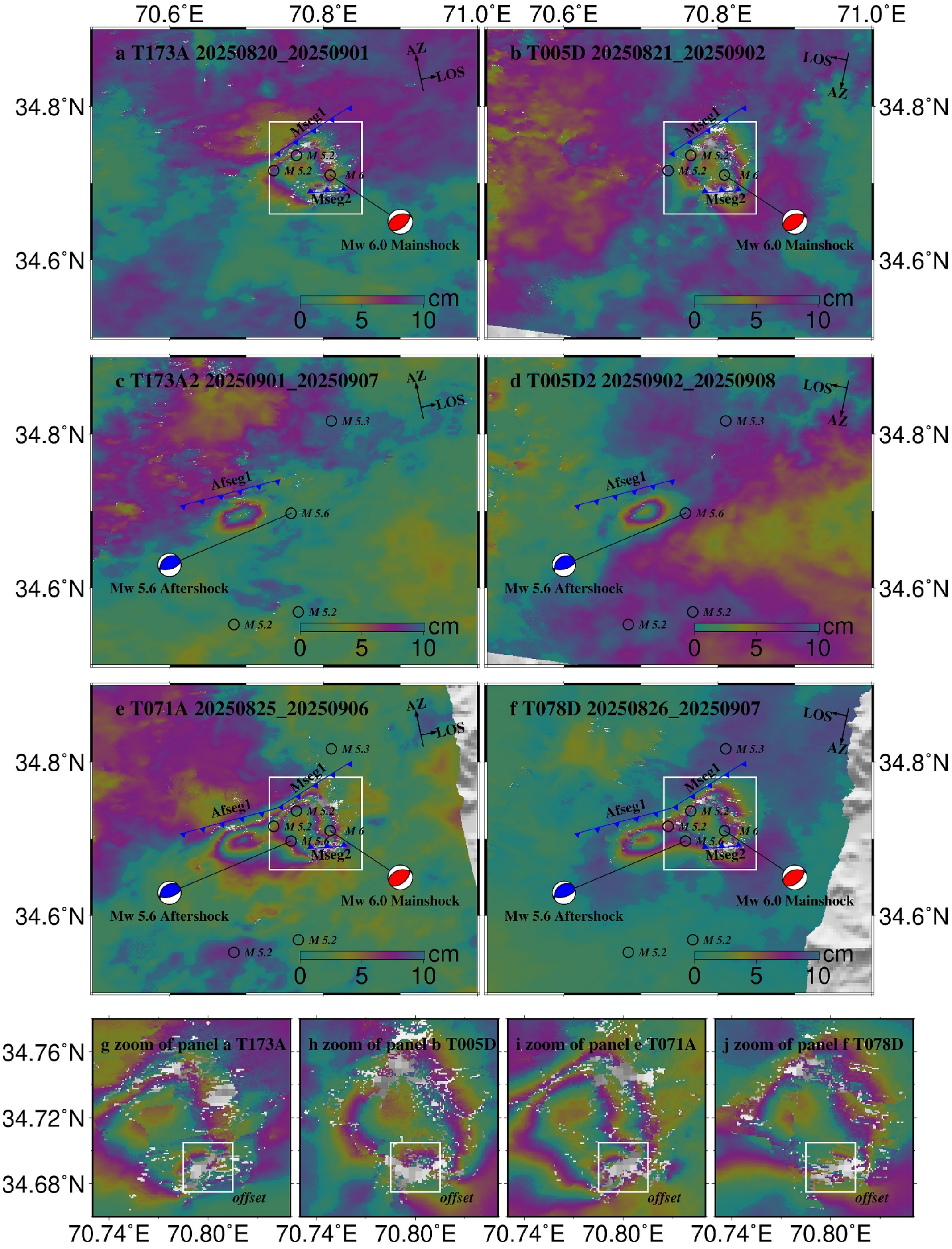

Figure 2. Mainshock and aftershock deformation derived from interferograms for the 2025 Asadabad earthquake sequence. Panels (a–f) show interferograms from different acquisition times and tracks of the Sentinel-1A satellite. Blue lines indicate the fault traces determined in this study, and black circles indicate the locations of the mainshock and aftershocks, from the USGS (2025). Panels (g, j) present enlarged views of the areas outlined by white rectangles in panels (a, b, e, and f), respectively, with the small white rectangle indicating the deformation offset region.

atmospheric delays were corrected using the Generic Atmospheric Correction Online Service for InSAR (GACOS; Yu et al., 2018). Additional details on interferogram construction and uncertainty estimates are provided in the Text S2 of Supporting Information S1.

2.2. Seismic Waveform Data and Modeling

To complement the geodetic constraints, we analyzed available seismic waveform data for the four principal earthquakes in the sequence. For the M 6.0 mainshock and the M 5.6 aftershock (USGS, 2025), teleseismic body-wave data with good signal-to-noise ratios and broad azimuthal coverage were inverted for focal mechanism, centroid depth, magnitude, and location using the Grond software package (Heimann et al., 2018), following established approaches (Craig et al., 2023; Craig & Hull, 2024).

For the two M 5.2 aftershocks (USGS, 2025), clear teleseismic signals were not detectable. Instead, we analyzed regional waveform data recorded at distances up to ∼1,400 km. Due to limited azimuthal coverage, these data were insufficient to independently resolve focal mechanisms. We therefore performed forward modeling using fault geometries inferred from InSAR data to test the consistency of candidate source models with the observed regional waveforms (see Text S3 in Supporting Information S1).

2.3. Fault Geometry and Slip Inversion

We performed geodetic source modeling using the Earthquake Cycle Analyses Toolkits (ECAT) package (He et al., 2025). Fault geometry was first explored using a Bayesian nonlinear inversion framework to identify the most probable fault orientations and dimensions consistent with the InSAR observations. Based on the preferred geometries and guided by seismological constraints, we then inverted for distributed slip on discretized fault surfaces. Full details of model parameterization, inversion settings, and uncertainty assessment are provided in the Text S4 in Supporting Information S1.

2.4. Interseismic Deformation From Time-Series InSAR

To investigate long-term deformation preceding the earthquake sequence, we analyzed Sentinel-1 time-series InSAR data spanning 2015–2024 using the LiCSAR–LiCSBAS processing workflow (Lazecký et al., 2020; Morishita et al., 2020). The resulting line-of-sight velocity fields provide regional-scale constraints on inter-seismic deformation patterns in the epicentral area. Processing details and validation procedures are described in the Text S5 in Supporting Information S1.

An AI-assisted language tool ChatGPT was used solely to improve the clarity and grammar of the manuscript. All scientific interpretations, analyses, and conclusions are the sole responsibility of the authors.

3. Results

3.1. Coseismic and Aftershock Deformation During the Earthquake Sequence

Figures 2a–2f presents interferograms showing the coseismic displacement field associated with the 2025 M 6.0 Asadabad earthquake sequence, which includes the M 6.0 mainshock and three M > 5 aftershocks within the deformation area (USGS, 2025). The observed line-of-sight (LOS) displacements range from −10 to 35 cm across all interferograms, respectively. For tracks T173A and T005D, the interferograms in subpanels (a–b) span the M 6.0 mainshock and the two M 5.2 aftershocks, whereas those in subpanels (c–d) record deformation related to the M 5.6 aftershock. In contrast, interferograms from tracks T071A and T078D (subpanels e–f) span all four earthquakes and therefore represent the cumulative deformation from the entire earthquake sequence, consistent with the temporal coverage and combined deformation recorded by the T173A and T005D interferograms (Figures S1–S2 in the Supporting Information S1).

In addition, zoomed views of the mainshock area (Figures 2g–2j) reveal a localized displacement offset at approximately 70.8°E, 34.69°N, confined to an area of roughly 3 × 3 km. This offset is consistently observed in multiple interferograms and indicates localized rupture within the mainshock rupture zone. When combined with the rupture associated with the M 5.6 aftershock, the InSAR observations collectively suggest that the earthquake sequence involved three distinct rupture segments.

3.2. Geodetic Fault Geometry and Seismic Waveform Nodal Plane Solution

To characterize the complex earthquake rupture, we inverted fault geometry using the T173A and T005D interferograms covering the mainshock assuming both single-fault (south-dipping) and two-fault (south dipping and north-dipping) configurations. The two-fault model provides a substantially improved fit to the observed deformation patterns (Table S3 and Figures S3–S7 in the Supporting Information S1), indicating that multiple faults ruptured across the earthquakes covered by this interferogram (the mainshock and two M 5.2 aftershocks (Figures 2a and 2b)). The preferred model consists of a main rupture segment (Mseg1) with a strike of 59° ± 1°, dip of 69° ± 1°, and rake of 122° ± 2°, and a secondary rupture segment (Mseg2) with a strike of 256° ± 1°, dip of 77° ± 3°, and rake of 116° ± 3° (Figure 2). Both segments are characterized by high-angle faulting with dominant reverse slip and a significant strike-slip component. The preferred two-fault model partitions the mainshock rupture into a dominant segment (Mseg1) with a seismic moment of $8.5 \pm 3.2 \times 10^{17}$ N·m, assuming a shear modulus of 3.0×10^{10} Pa (the same shear modulus is used throughout), yielding a magnitude of Mw 5.9. The secondary segment (Mseg2) with $1.1 \pm 0.4 \times 10^{17}$ N·m (i.e., Mw 5.3), indicating that the secondary rupture contributes ~10%–15% of the total moment release. We therefore suggest that mainshock ruptured on the south-dipping Mseg1 plane, while the following aftershocks (two M 5.2 events) likely ruptured on the separate, antithetic, north-dipping Mseg2 fault.

We further inverted the geometry of the M 5.6 aftershock using the later interferometric pairs T173A2 and T005D2 (Table S3 and Figures S8–S9 in the Supporting Information S1). The inferred aftershock rupture (Afseg1) has a strike of 52° ± 1°, dip of 79° ± 1°, and rake of 113° ± 3°, broadly consistent with the kinematics of the mainshock rupture segments. The inferred geometry of the M 5.6 aftershock (Afseg1) corresponds to an average slip of 1.85 ± 0.15 m over a rupture area of 4.75 ± 0.76 km^2, yielding a seismic moment of $2.6 \pm 0.4 \times 10^{17}$ N·m (i.e., Mw 5.5).

To complement our geodetic source inversions, we conduct body-waveform modeling of seismological data, as described in Section 2.2. Our seismological results suggest that the complex surface deformation is likely the product of two separate earthquakes, incorporating the coseismic displacements from both the mainshock and the M 5.6 aftershock (Figure 3a). Specifically, the mainshock segment Mseg1 exhibits a strike of 44° ± 6°, dip of 54° ± 2°, rake of 95° ± 5°, with a hypocentral depth of 7.6 ± 0.5 km and magnitude of 5.7, whereas the M 5.6 aftershock Afseg1 has a strike of 66° ± 40°, dip of 48° ± 4°, rake of 78° ± 9°, depth of 4.5 ± 0.4 km, and magnitude of 5.5 (uncertainties quoted are one standard deviation of the probability distribution).

Other smaller aftershocks, including the two M 5.2 earthquakes covered by T173A and T005D, are too small to independently constrain their focal mechanisms from teleseismic waveform data. To distinguish the rupture sequence between Mseg1 and Mseg2, we instead performed forward modeling using a focal mechanism based on the Mseg2 fault plane constrained by InSAR data, and compared the synthetic waveforms with sparse regional seismological observations (up to 1,400 km epicentral distance) from the two M 5.2 events (Figure 3b). As discussed in Section 3.2, the azimuthal data coverage at regional distances is insufficient to independently determine the focal mechanism robustly from seismological data alone. However, using the constrained mechanism of Mseg2, our forward models (with a free magnitude and location, but a pre-defined focal mechanism) show good agreement with observed regional waveform data (Figure 3), and consistent combined magnitudes with the geodetic moment estimate for Mseg2, supporting our suggestion that the Mseg2 sub-rupture is associated with the two M 5.2 events and likely represents early aftershocks shortly after the mainshock rupture on Mseg1.

3.3. Slip Distribution of the Earthquake Sequence

We invert our InSAR data to determine the coseismic slip distribution using the T071A and T078D interferograms to fully cover the three rupture segments associated with the 2025 Asadabad earthquake sequence. Each segment is characterized by a single dominant asperity that is well resolved by the data (Figures 4a–4d; Table S4 in Supporting Information S1). For the main rupture segment (Mseg1), slip exceeding 0.5 m is confined to an area of approximately 7 km × 11 km, with a peak slip of 1.5 m occurring at depths of 2–10 km. This segment yields a seismic moment of 9.9×10^{17} N·m, corresponding to Mw 5.9, with an estimated stress drop of 19 MPa based on the circular crack model of Brune (1970). For the largest aftershock rupture (Afseg1), slip exceeding 0.5 m occupies an area of ~5 km × 5 km, with a maximum slip of 1.1 m at depths of 2–5 km, yielding a seismic moment of 4.2×10^{17} N·m (Mw 5.7), slightly larger than the M 5.6 recorded by USGS, likely reflecting differences between geodetic and seismic magnitude estimates, with an estimated stress drop of 31 MPa. In each case, the depth distribution of slip matches well with the seismologically-determined centroid depths (7.6 and 4.5 km for Mseg1 and Afseg1 respectively). Notably, no significant slip is resolved at or near the surface along the main seismogenic fault for Mseg1, indicating that the mainshock rupture was blind.

a) Global body-waveform modelling for the Mw 6.0 mainshock and Mw 5.6 aftershock

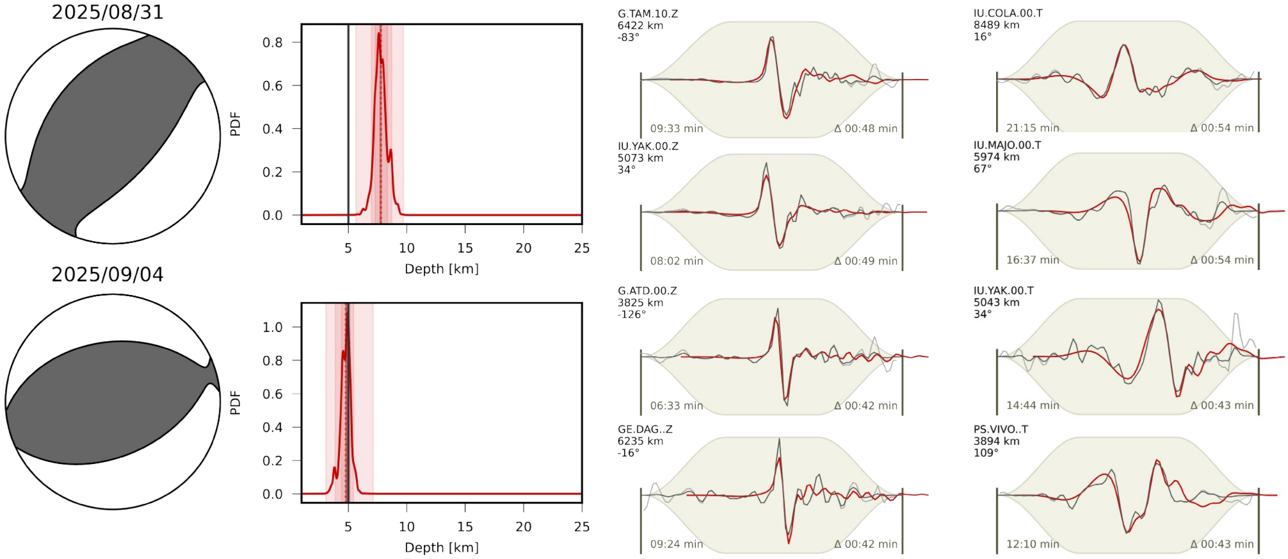

b) Local waveform forward modelling for the two Mw 5.2 aftershocks

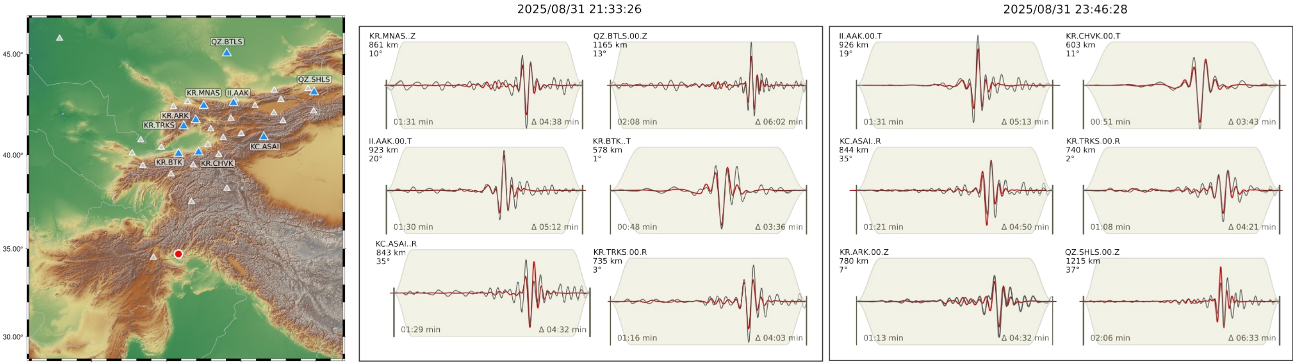

Figure 3. Results of seismological analysis. (a) Mainshock on 31 August 2025 and the large aftershock on 4 September 2025 using teleseismic waveform data. For each event, the probabilistic moment tensor, centroid depth probability density function, and selected example waveforms for the vertical and transverse components from different azimuths are shown. Observed waveforms are in black, and the best-fit synthetics are in red. Insets indicate station ID, epicentral distance, azimuth (above), and onset time with inversion window duration (below). (b) Local waveform forward modeling for the two M 5.2 aftershocks, based on the focal mechanism of the Mseg2 fault from this study. Observed waveforms are from stations highlighted in blue on the inset map.

The secondary rupture segment (Mseg2) exhibits a more compact slip patch, with slip exceeding 0.5 m distributed over an area of ∼3 km × 2 km and a peak slip of ∼0.7 m at shallow depths of 1–4 km. The inferred seismic moment for Mseg2 is 1.92×10^{17} N·m, corresponding to Mw 5.45, with an estimated stress drop of 85 MPa. Given the very shallow slip distribution and the presence of residual surface deformation associated with Mseg2, the rupture likely propagated close to the surface, suggesting that this secondary rupture may have been associated with localized surface or near-surface faulting.

Slip distributions constrained by the T173A and T005D data sets are shown in Figures S10–S20 of Supporting Information S1 for reference. Although variations in peak slip and spatial extent arise from differences in temporal coverage and geometric configuration among the data sets, all inversions consistently capture the primary characteristics of the three asperities. The distinct slip distribution patterns of the three segments are further supported by the checkerboard resolution test (Figure S21 in the Supporting Information S1).

Finally, we examined the sensitivity of the slip distribution to variations in the main fault dip (Figure 4e). For lower dip angles, modeled slip on Mseg1 would extend laterally toward the Kunar fault, implying geometric overlap between the two structures. Mseg1 is located within the hanging wall of the Kunar fault system and

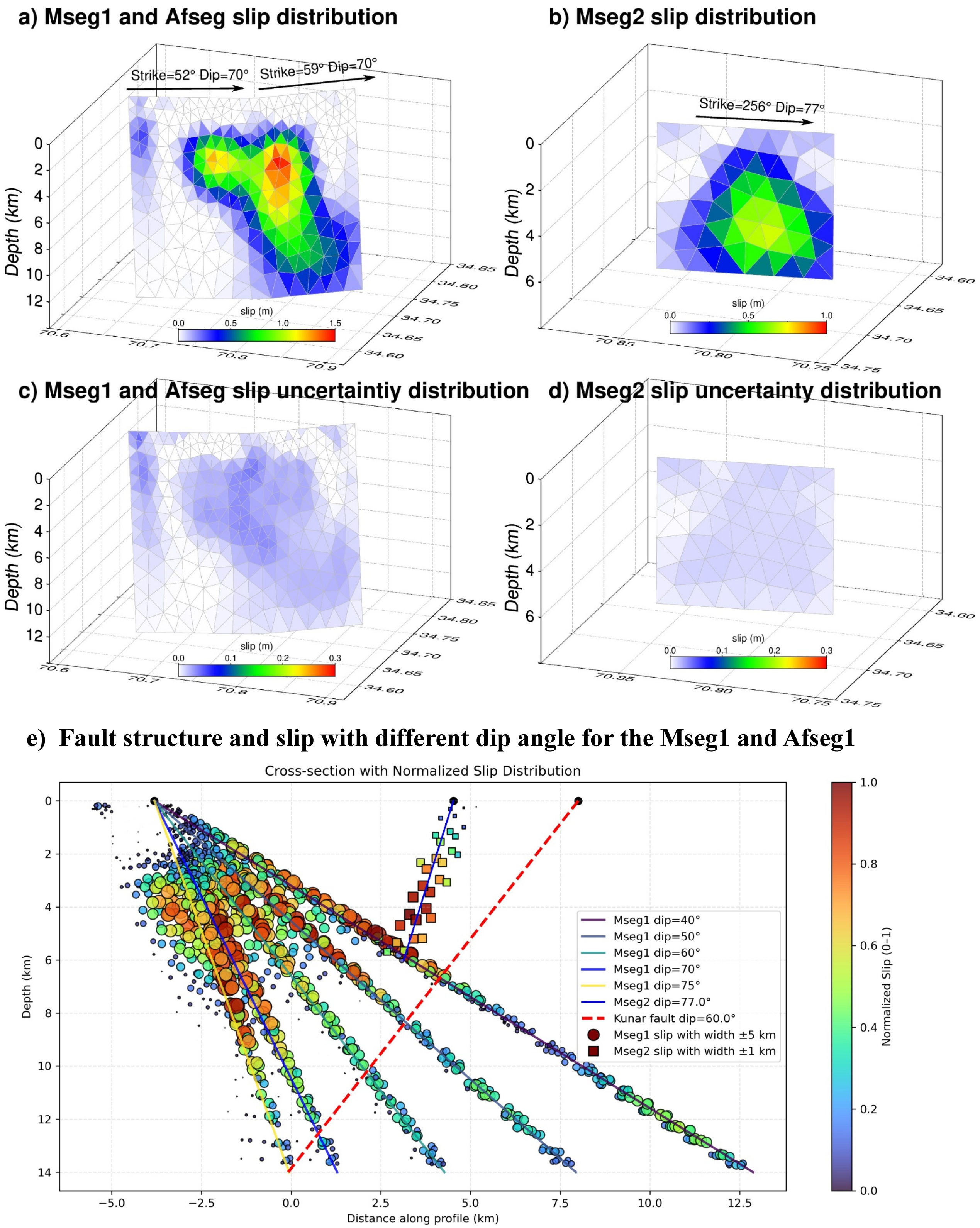

Figure 4. Slip distribution and local structural analysis. Slip distribution for the main fault (a) and the back-thrust secondary fault (b) during the earthquake sequence, and their uncertainties (c, d). (e) Slip cross-sections for varied dip-angle models of the main fault along a profile line (start: 70.740°E, 34.740°N; end: 70.783°E, 34.688°N) perpendicular to the main fault.

primarily accommodates deformation within the upper plate. Such a geometry implies that slip at depth is mainly accommodated by the Kunar fault rather than propagating downward across it (e.g., He et al., 2018). Therefore, lower dip-angle models that predict downward extension of slip are less consistent with this structural framework, and a steeper dip angle (~70°) provides a more geologically plausible representation of the main fault geometry.

3.4. Regional Interseismic Deformation Velocity

To explore potential pre-earthquake deformation that may have influenced the subsequent rupture sequence, we analyzed interseismic deformation rates across the study area using time-series InSAR. Time-series InSAR from both ascending and descending tracks indicate generally low LOS deformation rates across the study area, within −5 to 5 mm/yr (±0.5 mm/yr uncertainty), except in high-elevation regions affected by snow-induced decorrelation (Figures 5a and 5b). Localized subsidence is observed along alluvial valleys south of the Kunar fault and within the Jalalabad alluvial plain, forming banded to patchy patterns that closely follow surface geomorphology and are most likely related to hydrologically driven processes.

In contrast, a localized uplift anomaly is observed in the epicentral region between Mseg1 and Mseg2. The anomaly exhibits a roughly circular geometry with a diameter of ~3–5 km and LOS rates of ~2–5 mm/yr. A profile AA' extracted approximately parallel to the regional compressional direction (Figure 5c) shows a gradual increase in LOS velocity of ~1–2 mm/yr from SSE to NNW over ~36 km, where topographic relief varies modestly. In the epicentral region, LOS velocities increase sharply and then decrease over a shorter distance (~16 km), spatially coincident with an increase in relief but exhibiting only a weak overall correlation with topography. A perpendicular profile (BB'; Figure 5d) shows clear LOS displacement within the epicentral region but no comparable uplift signals on either the NE or SW sides, highlighting the spatial localization of the deformation. Taken together, these observations are consistent with localized interseismic LOS uplift of ~2 mm/yr centered on the epicentral region relative to its surrounding region (Assuming negligible north–south motion, equivalent to ~3 mm/yr vertical uplift and ~1 mm/yr westward motion;time series points analysis in Figure S22 in the Supporting Information S1). Although the inferred uplift signal is subtle, its spatial localization, consistency across viewing geometries, and lack of correlation with topography or seasonal variability argue against the signal being solely attributable to a processing artifact.

4. Discussion

4.1. Observations of Multi-Stage Shallow Ruptures

InSAR and gWFM analyses reveal a multi-stage shallow rupture at depths of ~4–5 km associated with the 2025 Mw 5.9 Asadabad earthquake in Afghanistan. The earthquake sequence exhibits a complex spatiotemporal rupture evolution: the mainshock ruptured the Mseg1 fault segment, followed within 2–4 hours by rupture of a secondary backthrust (Mseg2), manifested as two smaller M > 5.0 aftershocks from USGS (equivalent to a combined Mw 5.4 in this study). Four days later, an additional fault segment located southwest of the mainshock rupture area ruptured, producing the Mw 5.7 aftershock on Afseg1.

The secondary rupture on Mseg2 is inferred to have reached the surface. Although this surface-reaching rupture is not clearly expressed in the primary slip map (Figure 4b), residuals indicate localized misfits in this region (Figure S20f in Supporting Information S1), likely reflecting some effects in the joint inversion at small spatial scales. Importantly, discontinuities across the Mseg2 fault in the deformation signal observed in the InSAR data (Figures 2g–2j; Figure S2a in the Supporting Information S1) and the shallow slip distribution resolved in the inversion results from T173A and T005D data sets (Figure S13 in the Supporting Information S1). Based on the estimated moment accommodated on this fault segment, and the consistency of its orientation with regional seismic waveform data, we infer that this secondary fault most likely hosted the two smaller aftershocks, shortly following the Mw 5.9 mainshock.

Coulomb stress calculations (Text S6; Figure S23 in Supporting Information S1) further indicate that Mseg2 is in a region of positive stress change induced by Mseg1, supporting the idea that the secondary rupture was promoted by stress transfer from the mainshock. Similarly, Afseg1 lies within a region of positive Coulomb stress change resulting from the combined stress of Mseg1 and Mseg2, suggesting that its rupture was facilitated by sequential stress interactions. These results provide quantitative support for the observed temporal sequence of sub-events and the spatial distribution of shallow ruptures.

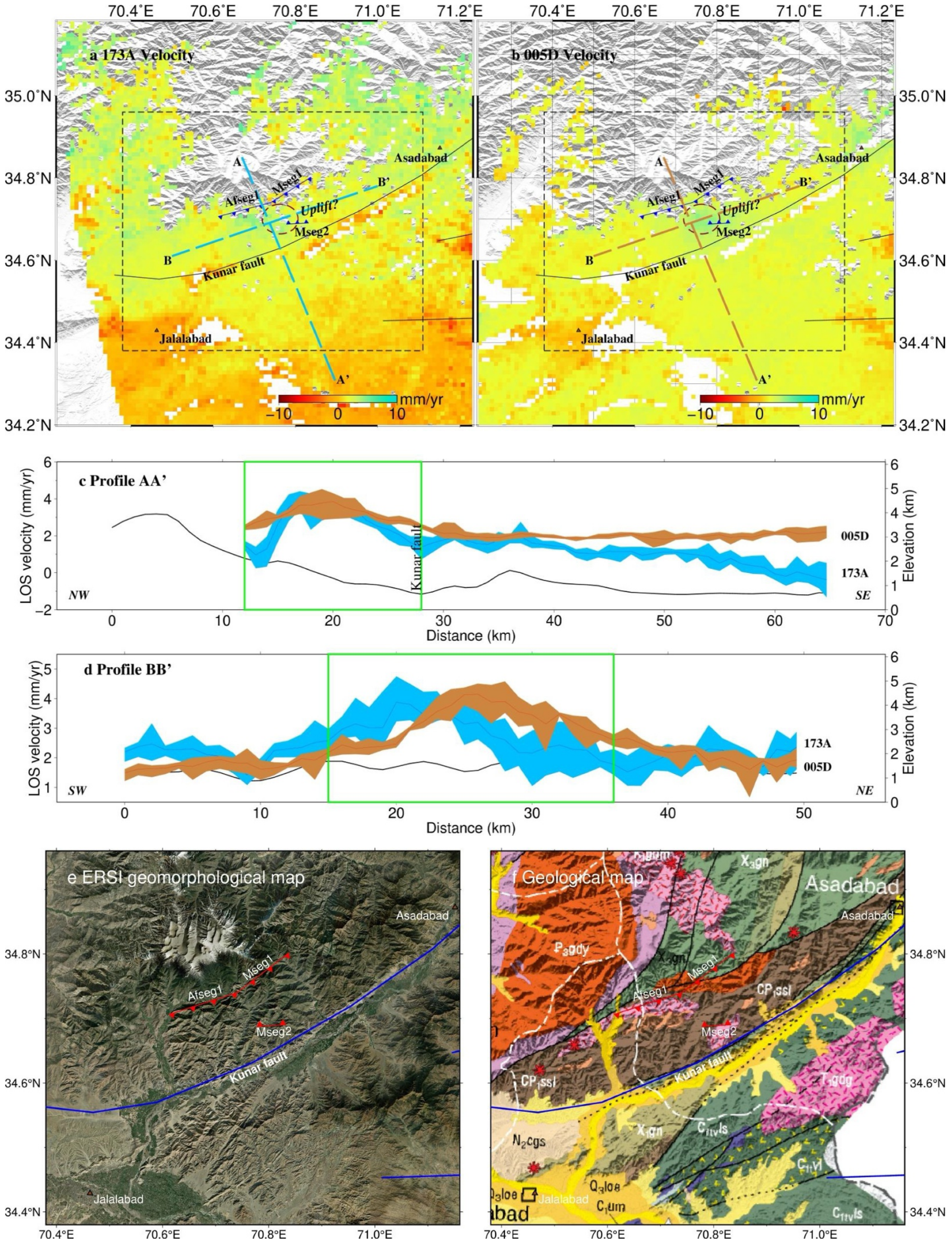

Figure 5. Interseismic InSAR and regional geology and geomorphology. (a, b) Time-series InSAR velocity maps from ascending and descending tracks. (c, d) Relationship between deformation rates and topography along profile AA' and BB', respectively. (e) Optical geomorphology of the region from ESRI (Environmental Systems Research Institute, 2023). (f) Regional geological map from ESCAP, United Nations (1995). Olivine-green denotes gneisses (X_3gn), brown denotes granite (CP_1ssl), pink denotes minor intercalated sandstones (T1gdg), and yellow denotes Holocene sandstone (Q_4a). The rupture fault traces (Mseg1, Mseg2, and Afseg1) for the 2025 sequence are from this study. Dark red triangles mark the major cities in the epicentral region, including Asadabad and Jalalabad.

Although multi-segment ruptures are common in large earthquakes (e.g., Hamling et al., 2017; Liu et al., 2023), these events typically involve surface-rupturing mainshocks associated with major plate-scale faults. In contrast, earthquake sequences in which a buried mainshock is followed by shallow or surface-reaching aftershocks are relatively rare; a notable example is the 2024 Mw 7.0 Wushi earthquake, where shallow backthrust aftershocks locally ruptured the surface (Li et al., 2025; Yin et al., 2025). Despite its moderate magnitude (Mw 5.9), the Asadabad sequence exhibits an unusually complex rupture evolution, involving multiple rupture stages, localized surface or near-surface rupture on secondary backthrust faults, and notably delayed aftershock rupture along the main fault (i.e., Mseg1). These features imply prolonged fault interaction and progressive stress redistribution within the shallow crust of an orogenic interior.

4.2. Pre-event Deformation for the 2025 Asadabad Earthquake Sequence

Time-series InSAR observations reveal localized interseismic uplift of ~2 mm/yr prior to the 2025 Asadabad earthquake, spatially coincident with the epicentral region. Vertical deformation in Central Asia reflects a combination of tectonic uplift and hydrologically driven subsidence in arid regions, where groundwater extraction and prolonged drought have intensified over the past decade (He et al., 2024; Ou et al., 2025; Payne et al., 2025). In the Asadabad area, widespread subsidence occurs along the Kunar fault, whereas the epicentral region exhibits localized uplift, distinct from surrounding deformation patterns.

Localized uplift and abrupt vertical offsets are commonly linked to shallow fluid-related pre-slip or slow aseismic deformation, which can modulate shallow crustal stress and facilitate seismic rupture in orogenic interiors (Johnson et al., 2025; McGrath et al., 2025; Ou et al., 2025; Shen & Liu, 2025). Notably, the 2025 Asadabad earthquake did not occur on previously identified active faults. In this context, the observed localized uplift may reflect shallow crustal deformation processes, potentially involving fault-zone compaction or fluid-related effects. Such processes could have contributed to local stress perturbations, although their role in promoting the subsequent multi-stage shallow rupture sequence remains uncertain (Yun et al., 2025).

4.3. Amplified Hazard From Unmapped Fault Damage Zones

The Asadabad earthquake occurred within crystalline basement rocks dominated by gneiss and granite, without association with mapped Quaternary faults (Figure 5g). Lithological heterogeneities favor distributed fracture networks and fault damage zones, which can host cascading slip (Collettini et al., 2022; Palgunadi et al., 2024). Accordingly, the severe damage caused by the Mw 5.9 earthquake is best explained by rupture of a shallow, network-style fracture system. This system is interpreted as an immature fault system, defined as a distributed and poorly localized fault network that lacks well-developed, throughgoing fault planes and is characterized by diffuse deformation (e.g., Faulkner et al., 2010; Scholz, 2019), producing spatially distributed near-surface deformation (Li et al., 2025; Yin et al., 2025).

Our InSAR and modeling results indicate that slip was shallow and spatially concentrated, with elevated stress drops exceeding the typical crustal range (~1–10 MPa; Kanamori & Anderson, 1975), likely enhancing near-surface ground shaking. Available reports also indicate that vulnerable non-engineered buildings contributed substantially to structural damage (WHO, 2025), and possible site amplification within the Jalalabad basin may have further increased ground motion. These combined factors explain why, despite its moderate magnitude, the earthquake caused over 2,200 fatalities, illustrating that earthquakes on unmapped or distributed fault systems in basement rocks can generate destructive shallow rupture. This case highlights the limitations of magnitude-based hazard assessments and underscores the importance of considering fault damage zones, rupture complexity, and site effects in seismic risk evaluation.

5. Conclusions

By integrating InSAR observations with teleseismic waveform modeling, we resolve the deformation and rupture processes of the 2025 Mw 5.9 Asadabad earthquake. The sequence involved complex, multi-stage rupture, including a blind mainshock rupture, shallow secondary backthrusting, and a delayed rupture on the main fault. Slip was predominantly shallow, with near-surface deformation on secondary fault segments. InSAR time series reveal localized pre-event uplift near the epicenter, suggesting shallow deformation preceding the earthquake. The rupture occurred on an unmapped, immature fault system within crystalline basement rocks, consistent with cascading failure within a fault damage zone. These results help explain the severe damage produced by this moderate-magnitude event and underscore the limitations of magnitude-based seismic hazard assessments in orogenic interiors.

Conflict of Interest

The authors declare no conflicts of interest relevant to this study.

Availability Statement

The ECAT code (He et al., 2025) used for the nonlinear and linear slip inversion is available at Zenodo (https://doi.org/10.5281/zenodo.13730101). The Sentinel-1 SAR data were provided by the European Space Agency (ESA, 2025) and are available via Copernicus Data Space Ecosystem (https://dataspace.copernicus.eu/). The Copernicus Digital Elevation Model provided by the European Space Agency is available at https://doi.org/10.5270/ESA-c5d3d65. Interferograms used for time-series analysis are available from the Centre for the Observation and Modelling of Earthquakes and Tectonics (COMET, 2025) data portal (https://comet.nerc.ac.uk/comet-lics-portal/). Earthquake catalogs used in this study are available from the U.S. Geological Survey (https://earthquake.usgs.gov/earthquakes), and the Global Centroid Moment Tensor (https://www.globalcmt.org, GCMT, 2025). Seismological waveform data were obtained from the EarthScope Data Center (IRIS DMC, 2025; https://service.iris.edu), last accessed 18 December 2025. Figures were generated using the Generic Mapping Tools (GMT) software (Wessel et al., 2019). All data used in this study are publicly available.

Acknowledgments

We sincerely thank the Editors and the two anonymous reviewers for their constructive comments and suggestions. This work was supported by the National Natural Science Foundation of China (42174004 and 42374003). COMET is the UK NERC Centre for the Observation and Modelling of Earthquakes, Volcanoes and Tectonics, a partnership between UK universities and the British Geological Survey. Tim Craig was supported in this work by the Royal Society under URF/R1/180088 and URF/R/231019.

References

Brune, J. N. (1970). Tectonic stress and the spectra of seismic shear waves from earthquakes. *Journal of Geophysical Research*, *75*(26), 4997–5009. https://doi.org/10.1029/jb075i026p04997

Collettini, C., Barchi, M. R., De Paola, N., Trippetta, F., & Tinti, E. (2022). Rock and fault rheology explain differences between on fault and distributed seismicity. *Nature Communications*, *13*(1), 5627. https://doi.org/10.1038/s41467-022-33373-y

COMET. (2025). LiCSAR InSAR products [Dataset]. *Centre for the Observation and Modelling of Earthquakes and Tectonics*. Retrieved from https://comet.nerc.ac.uk/comet-lics-portal/

Craig, T., & Hull, A. (2024). Extensional failure in a weak slab under slab pull--the 2023 Mw 6.4 Quiché, Guatemala, earthquake. *Seismica*, *3*(1). https://doi.org/10.26443/seismica.v3i1.1190

Craig, T. J., Jackson, J., Priestley, K., & Ekström, G. (2023). A Cautionary Tale: Examples of the mis-location of small earthquakes beneath the Tibetan plateau by routine approaches. *Geophysical Journal International*, *233*(3), 2021–2038. https://doi.org/10.1093/gji/ggad025

EarthScope Data Center (IRIS DMC). (2025). Seismological waveform data [Dataset]. Retrieved from https://service.iris.edu

Economic and Social Commission for Asia and the Pacific (ESCAP), UN. (1995). *Geology and mineral resources of Afghanistan*. United Nations. Retrieved from https://hdl.handle.net/20.500.12870/4219

Environmental Systems Research Institute (ESRI). (2023). ArcGIS online. Retrieved from https://www.esri.com

European Space Agency (ESA). (2023). Copernicus Digital Elevation Model (DEM) [Dataset]. https://doi.org/10.5270/ESA-c5d3d65

European Space Agency (ESA). (2025). Sentinel-1 Synthetic Aperture Radar (SAR) data [Dataset]. *Copernicus Data Space Ecosystem*. Retrieved from https://dataspace.copernicus.eu/

Faulkner, D. R., Jackson, C. A. L., Lunn, R. J., Schlische, R. W., Shipton, Z. K., Wibberley, C. A. J., & Withjack, M. O. (2010). A review of recent developments concerning the structure, mechanics and fluid flow properties of fault zones. *Journal of Structural Geology*, *32*(11), 1557–1575. https://doi.org/10.1016/j.jsg.2010.06.009

Geological Survey, U. S. (2025). Events M 5.0 in the Pamir–Himalayan syntaxis region since 1900-01-01 [Dataset]. https://earthquake.usgs.gov/earthquakes

Global Centroid Moment Tensor (GCMT). (2025). Global CMT earthquake catalog [Dataset]. Retrieved from https://www.globalcmt.org

Hamling, I. J., Hreinsdóttir, S., Clark, K., Elliott, J., Liang, C., Fielding, E., et al. (2017). Complex multifault rupture during the 2016 Mw 7.8 Kaikōura earthquake, New Zealand. *Science*, *356*(6334), eaam7194. https://doi.org/10.1126/science.aam7194

He, K. F., Xu, G. Y., Sun, L. X., Xu, C. J., & Wen, Y. M. (2025). ECAT: Integrated nonlinear and linear inversion for complex fault systems and slip distribution (Version 1.5.0) [Software]. *Zenodo*. https://doi.org/10.5281/zenodo.13730101

He, P., Hetland, E. A., Niemi, N. A., Wang, Q., Wen, Y., & Ding, K. (2018). The 2016 Mw 6.5 Nura earthquake in the Trans Alai range, northern Pamir: Possible rupture on a back-thrust fault constrained by Sentinel-1A radar interferometry. *Tectonophysics*, *749*, 62–71. https://doi.org/10.1016/j.tecto.2018.10.025

He, P., Wen, Y., Zhong, Y., & Cai, J. (2024). Nonoverlapped Sources of the Devastating 2023 M w> 6 Herat, Afghanistan, Earthquake Swarm estimated by InSAR. *Seismological Research Letters*, *96*(2A), 838–847. https://doi.org/10.1785/0220240239

Heimann, S., Isken, M., Kühn, D., Sudhaus, H., Steinberg, A., Daout, S., et al. (2018). Grond: A probabilistic earthquake source inversion framework [Software]. https://doi.org/10.5880/GFZ.2.1.2018.003

Johnson, B., Elliott, J. R., Yetirmishli, G., Javanshir, R., Kazimova, S., Kazimov, I., et al. (2025). Fault creep in the fluid-rich Kura Basin, Azerbaijan, imaged with InSAR. *Geophysical Journal International*, *243*(2), ggaf320. https://doi.org/10.1093/gji/ggaf320

Kanamori, H., & Anderson, D. L. (1975). Amplitude of the Earth's free oscillations and long-period characteristics of the earthquake source. *Journal of Geophysical Research*, *80*(8), 1075–1078. https://doi.org/10.1029/jb080i008p01075

Kapp, P., & DeCelles, P. G. (2019). Mesozoic–Cenozoic geological evolution of the Himalayan-Tibetan orogen and working tectonic hypotheses. *American Journal of Science*, *319*(3), 159–254. https://doi.org/10.2475/03.2019.01

Kufner, S. K., Bie, L., Gao, Y., Lindner, M., Waizy, H., Kakar, N., & Rietbrock, A. (2023). The devastating 2022 M6.2 Afghanistan earthquake: Challenges, processes, and implications. *Geophysical Research Letters*, *50*(11), e2022GL102176. https://doi.org/10.1029/2022GL102176

Kufner, S. K., Kakar, N., Bezada, M., Bloch, W., Metzger, S., Yuan, X., et al. (2021). The Hindu Kush slab break-off as revealed by deep structure and crustal deformation. *Nature Communications*, *12*(1), 1685. https://doi.org/10.1038/s41467-021-21760-w

Kufner, S. K., Schurr, B., Haberland, C., Zhang, Y., Saul, J., Ischuk, A., & Oimahmadov, I. (2017). Zooming into the Hindu Kush slab break-off: A rare glimpse on the terminal stage of subduction. *Earth and Planetary Science Letters*, *461*, 127–140. https://doi.org/10.1016/j.epsl.2016.12.043

Lazecký, M., Spaans, K., González, P. J., Maghsoudi, Y., Morishita, Y., Albino, F., et al. (2020). LiCSAR: An automatic InSAR tool for measuring and monitoring tectonic and volcanic activity. *Remote Sensing*, *12*(15), 2430. https://doi.org/10.3390/rs12152430

Li, H., Pan, J., Chevalier, M. L., Liu, D., Wang, S., Luo, H., et al. (2025). Aftershock-induced surface ruptures overshadow the 2024 Mw 7.0 Wushi mainshock, China. *Geology*, *54*(2), 105–110. https://doi.org/10.1130/G54078.1

Liu, C., Lay, T., Wang, R., Taymaz, T., Xie, Z., Xiong, X., et al. (2023). Complex multi-fault rupture and triggering during the 2023 earthquake doublet in southeastern Türkiye. *Nature Communications*, *14*(1), 5564. https://doi.org/10.1038/s41467-023-41404-5

McGrath, J. D., Elliott, J. R., Watson, A. R., Wright, T. J., Piazolo, S., & Hamling, I. J. (2025). Linking geodetically resolved uplift to long-term orogenic exhumation in the Southern Alps, New Zealand. *Journal of Geophysical Research: Solid Earth*, *130*(11), e2024JB030625. https://doi.org/10.1029/2024JB030625

Mohadjer, S., Ehlers, T. A., Bendick, R., Stübner, K., & Strube, T. (2016). A Quaternary fault database for central Asia. *Natural Hazards and Earth System Sciences*, *16*(2), 529–542. https://doi.org/10.5194/nhess-16-529-2016

Morishita, Y., Lazecky, M., Wright, T. J., Weiss, J. R., Elliott, J. R., & Hooper, A. (2020). LiCSBAS: An open-source InSAR time series analysis package integrated with the LiCSAR automated Sentinel-1 InSAR processor. *Remote Sensing*, *12*(3), 424. https://doi.org/10.3390/rs12030424

NOAA - National Oceanic and Atmospheric Administration. (2023). *National Centers for Environmental Information*. Retrieved from https://www.ngdc.noaa.gov/hazel/view/hazards/earthquake/search

Ou, Q., Elliott, J., Maghsoudi, Y., Rollins, C., Lazecky, M., & Wright, T. (2025). Extension of Tian Shan along a nascent shear zone. https://doi.org/10.21203/rs.3.rs-7529996/v1

Palgunadi, K. H., Gabriel, A. A., Garagash, D. I., Ulrich, T., & Mai, P. M. (2024). Rupture dynamics of cascading earthquakes in a multiscale fracture network. *Journal of Geophysical Research: Solid Earth*, *129*(3), e2023JB027578. https://doi.org/10.1029/2023JB027578

Payne, J. A., Watson, A. R., Maghsoudi, Y., Ebmeier, S. K., Rigby, R., Lazecký, M., et al. (2025). Widespread extent of irrecoverable aquifer depletion revealed by country-wide analysis of land surface subsidence hazard in Iran. *Journal of Geophysical Research: Solid Earth*, *130*(9), e2024JB030367. https://doi.org/10.1029/2024JB030367

Rollins, C. (2023). earjcr1/AHB_GPS: V0.1 (v0.1) [Dataset]. *Zenodo*. https://doi.org/10.5281/zenodo.10372924

Ruleman, C. A., Crone, A. J., Machette, M. N., Haller, K. M., & Rukstales, K. S. (2007). Probable and possible Quaternary faults of Afghanistan [USGS open-file report 1103]. GIS and PDF files are Retrieved from http://pubs.usgs.gov/of/2007/1103

Scholz, C. H. (2019). *The mechanics of earthquakes and faulting*. Cambridge University Press. https://doi.org/10.1017/9781316681473

Shen, Z. K., & Liu, Z. (2025). GNSS and InSAR integration for 3-D crustal deformation in California and western Nevada. *Journal of Geophysical Research: Solid Earth*, *130*(11), e2024JB030888. https://doi.org/10.1029/2024JB030888

Shnizai, Z. (2020). Mapping of active and presumed active faults in Afghanistan by interpretation of 1-arcsecond SRTM anaglyph images. *Journal of Seismology*, *24*(6), 1131–1157. https://doi.org/10.1007/s10950-020-09933-4

Sippl, C., Schurr, B., Yuan, X., Mechie, J., Schneider, F. M., Gadoev, M., et al. (2013). Geometry of the Pamir-Hindu Kush intermediate-depth earthquake zone from local seismic data. *Journal of Geophysical Research: Solid Earth*, *118*(4), 1438–1457. https://doi.org/10.1002/jgrb.50128

Styron, R., & Pagani, M. (2020). The GEM global active faults database. *Earthquake Spectra*, *36*(1S), 160–180. https://doi.org/10.1177/8755293020944182

Tapponnier, P., Xu, Z., Roger, F., Meyer, B., Arnaud, N., Wittlinger, G., & Yang, J. (2001). Oblique stepwise rise and growth of the Tibet Plateau. *Science*, *294*(5547), 1671–1677. https://doi.org/10.1126/science.105978

Wegnüller, U., Werner, C., Strozzi, T., Wiesmann, A., Frey, O., & Santoro, M. (2016). Sentinel-1 support in the GAMMA software. *Procedia Computer Science*, *100*, 1305–1312. https://doi.org/10.1016/j.procs.2016.09.246

Wessel, P., Luis, J. F., Uieda, L., Scharroo, R., Wobbe, F., Smith, W. H. F., & Tian, D. (2019). The Generic Mapping Tools (GMT) version 6 [Software]. *Geochemistry, Geophysics, Geosystems*, *20*(11), 5556–5564. https://doi.org/10.1029/2019GC008515

World Health Organization (WHO). (2025). Earthquake in Eastern Afghanistan. Reporting period: Based on available information as of 15:00 on 2 October 2025. Retrieved from https://www.emro.who.int/images/stories/afghanistan/afghanistan-earthquake-sitatuion-report-13-2-october-2025.pdf

Yin, A., & Harrison, T. M. (2000). Geologic evolution of the Himalayan-Tibetan orogen. *Annual Review of Earth and Planetary Sciences*, *28*(1), 211–280. https://doi.org/10.1146/annurev.earth.28.1.211

Yin, X., Li, T., Zhang, Y., Peng, Z., Dal Zilio, L., Chen, Z., et al. (2025). Interlacing ruptures of the 2024 Wushi earthquake (Chinese Tian Shan) controlled by structural inheritance. *Communications Earth & Environment*, *6*(1), 908. https://doi.org/10.1038/s43247-025-02855-4

Yu, C., Li, Z., Penna, N. T., & Crippa, P. (2018). Generic atmospheric correction model for interferometric synthetic aperture radar observations. *Journal of Geophysical Research: Solid Earth*, *123*(10), 9202–9222. https://doi.org/10.1029/2017JB015305

Yun, J., Gabriel, A. A., May, D. A., & Fialko, Y. (2025). Controls of dynamic and static stress changes and aseismic slip on delayed earthquake triggering: Application to the 2019 Ridgecrest earthquake sequence. *Journal of Geophysical Research: Solid Earth*, *130*(12), e2025JB031271. https://doi.org/10.1029/2025JB031271

References From the Supporting Information

Elliott, J. R., Fang, J., Lazecký, M., Maghsoudi, Y., Ou, Q., Payne, J. A., et al. (2026). Deformation, strains and velocities for the Alpine Himalayan Belt from trans-continental Sentinel-1 InSAR & GNSS. *Remote Sensing of Environment*, *338*, 115320. Article 115320. https://doi.org/10.1016/j.rse.2026.115320

Jolivet, R., Jara, J., Dalaison, M., Rouet-Leduc, B., Özdemir, A., Dogan, U., et al. (2023). Daily to centennial behavior of aseismic slip along the central section of the North Anatolian Fault. *Journal of Geophysical Research: Solid Earth*, *128*(7), e2022JB026018. https://doi.org/10.1029/2022JB026018

Stark, P. B., & Parker, R. L. (1995). Bounded-variable least-squares: An algorithm and applications. *Computational Statistics*, *10*, 129-129.

Toda, S., Stein, R. S., Richards-Dinger, K., & Bozkurt, S. B. (2005). Forecasting the evolution of seismicity in southern California: Animations built on earthquake stress transfer. *Journal of Geophysical Research*, *110*(B5). https://doi.org/10.1029/2004JB003415